Supplementary Information for: Super-resolution Orthogonal Deterministic Imaging Technique for Terahertz Subwavelength Microscopy

Hichem Guerboukha[1], Yang Cao[1], Kathirvel Nallappan[1,2], and Maksim Skorobogatiy[1,*]
[1]Engineering physics, Polytechnique Montréal, Montréal, Canada
[3]Electrical engineering, Polytechnique Montréal, Montréal, Canada
maksim.skorobogatiy@polymtl.ca

A. Terahertz imaging system

The amplitude and phase images were obtained using a standard THz time-domain spectroscopy (THz-TDS) imaging system [Fig. S1]. An ultrafast Ti:Sapphire laser (Spectra-physics, 800 nm, 100 MHz, 100fs) delivered 300 mW of optical power to an interdigitated photoconductive antenna (BATOP) for THz emission, and 10 mW to a wrapped dipole antenna (Menlo) for detection. The THz was focused on the object and the modulating mask under imaging using a pair of parabolic mirrors. The object was placed on a movable 3D micro-positioning stage and raster-scanned for imaging. An optical delay line was placed on the emitter side and the detected photocurrent was proportional to the electric field of the THz pulse. A Fourier transform of this electric field provided amplitude and phase spectra over a large bandwidth.

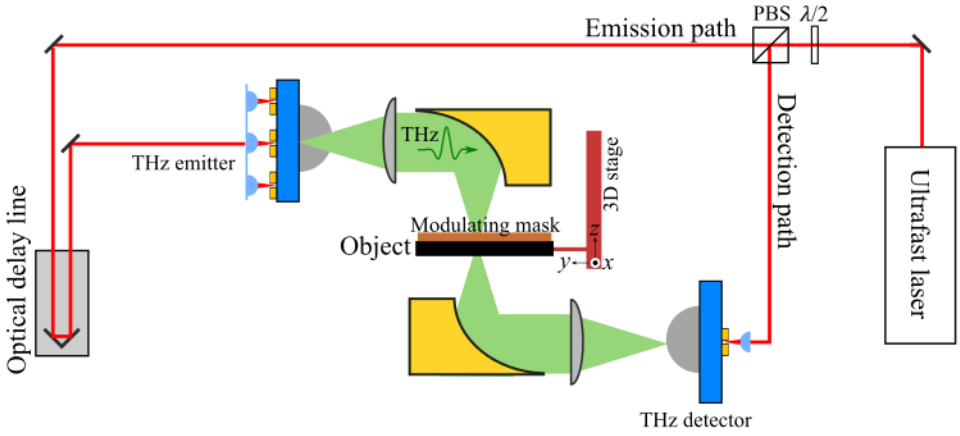

Fig. S1 THz time-domain spectroscopy system used to obtain spectral amplitude and phase images.

B. Fabrication of the object and the masks

In our experiments, the binary metal object representing the fleur-de-lys was made using toner-assisted metal foil transfer, also known as hot stamping [Fig. S2a]. This technique allows to fabricate metallic features directly on a paper substrate using a metal foil composite deposited on a thin layer of thermoplastic. The design was first printed on paper with a conventional office laser printer. The metallic foil composite (Therm O Web Deco Foil) was then placed on top of the print and both passed through a laminator. Due to enhanced local heating, the toner and thermoplastic are bonded, leading to a direct imprint of the metal layer on top of the printed design.

The phase masks were fabricated using fused deposition modeling (3D printing) of a polylactic acid (PLA) with refractive index of ~1.6. The phase elements $+1$ and -1 were obtained by varying the thickness from 1000 µm to 1800 µm, corresponding to 0 and π phase variations at 0.32 THz [Fig. S2b]. The amplitude masks were fabricated using the hot stamping technique discussed above [Fig. S2c].

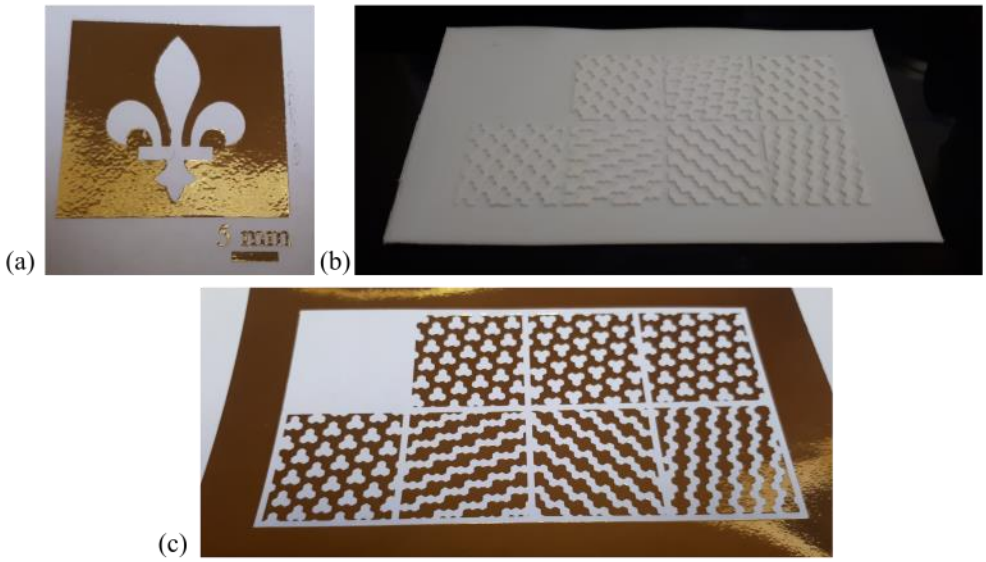

Fig. S2 (a) Fleur-de-lys object obtained using the hot stamping technique. The bar size is 5 mm. (b) A set of eight pure phase masks for second order SODI fabricated from PLA using fused deposition modeling. (c) A set of eight binary amplitude masks for second order SODI fabricated using toner-assisted metal foil transfer.

C. Determination of the size of the group of pixels in relation to the point spread function

In the SODI algorithm, the local orthogonality condition is used for the basic pixel group that has a characteristic size comparable to that of the imaging system point spread function (PSF). The basic pixel group is then periodically patterned to cover the whole object.

To determine the size of the basic pixel group for mask construction, we first need to measure the size of the imaging system PSF. For that, we performed a knife-edge measurement of the focused THz beam. We positioned a metal object (knife) in the focal plane and we moved it along the x direction while recording the THz field amplitude as a function of frequency [Fig. S3a]. In the x direction, we assume that the electric field amplitude can be represented with a Gaussian function with a standard deviation σ:

$$S(x) = A \exp\left[-\frac{(x - x_0)^2}{2\sigma^2}\right] \tag{S1}$$

where A is a normalization parameter and x_0 accounts for the center position of the Gaussian. The part of the beam that is measured (that is not blocked by the knife) is then given by the cumulative distribution function of the Gaussian function[1]:

$$\Phi(x) = A\int_{-\infty}^{x} \exp\left[-\frac{(x' - x_0)^2}{2\sigma^2}\right] dx' = \frac{A}{2}\left[1 + \mathrm{erf}\left(\frac{x - x_0}{\sigma\sqrt{2}}\right)\right] \tag{S2}$$

where x' can be seen as the position of the knife in the focal plane. The function $\mathrm{erf}(\xi)$ is the error function defined as:

$$\mathrm{erf}(\xi) = \frac{2}{\sqrt{\pi}}\int_0^{\xi} e^{-t^2} dt \tag{S3}$$

Using Eq. (S2) for every frequency, we fit the measurements using the error function [Eq. (S2)] and retrieve the σ parameter of the corresponding Gaussian distribution. We show in Fig. S3b the obtained σ parameter as a function of the wavelength (black dots). The red line is the theoretical estimate of the diffraction-limited Gaussian beam waist size[2]:

$$\sigma(\lambda) = \frac{\sqrt{2}}{\pi}\frac{F_m}{D_m}\lambda \tag{S4}$$

where in our case $F_m = 101.6$ mm is the focal length of the parabolic mirror and $D_m = 50.8$ mm is its diameter. The good fit between our experimental data and Eq. (S4) indicates that our system is limited by diffraction.

In the experiments, the basic group of pixels was made of 7 hexagons with an inter-pixel distance of 2 mm. To better visualize how the Gaussian PSF is related in size to the basic group of pixels, we show in Fig. S3c the amplitude of the Gaussian PSF [Eq. (S1)] for the different frequencies considered in the experiments, where σ was obtained from the measurements of Fig. S3b. The bold white circle and the dashed white circle correspond to circles of radius 2σ and 3σ respectively. Within these circles, 95% (2σ) and 99.7% (3σ) of the Gaussian beam amplitude is located. As we can see, for the frequency of 0.32 THz, the basic group of pixels is inscribed inside the circle of 3σ radius.

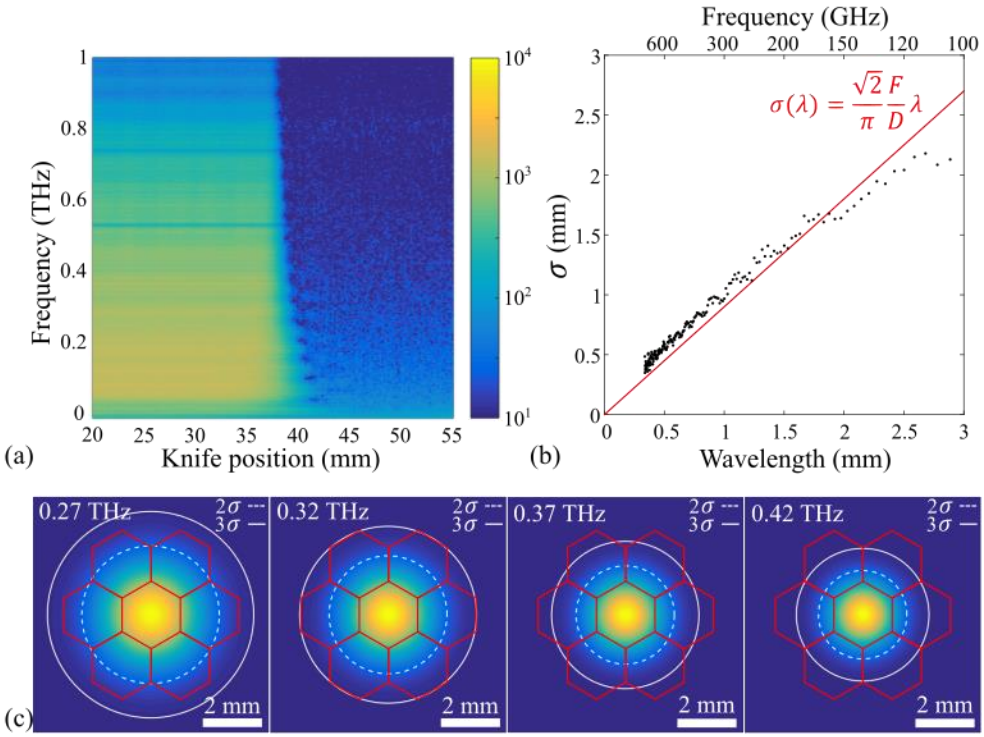

Fig. S3 (a) Knife-edge measurements. Electric field spectral amplitude as a function of the position of the knife in the focal plane. (b) Standard deviation σ as a function of the wavelength. The good fit between the measurements (black dots) and the fit (red line, $\sigma(\lambda) = \frac{\sqrt{2}}{\pi}\frac{F}{D}\lambda$) indicates that the beam is diffraction-limited according to Gaussian beam theory. (c) The basic pixel group used in our experiments and the Gaussian beam distribution for different frequencies.

D. Reconstruction of the phase for binary amplitude masks

In Section 4 of the main paper, we showed second order SODI reconstruction using binary amplitude masks. In particular, Fig. 3d showed the SODI reconstruction of the amplitude. In this section, we present the phase reconstruction using the same data. The original phase images for different frequencies are shown in the top row of Fig. S4, while the SODI reconstructions when considering the phase of $\langle E^2(\vec{r})\rangle - \langle E(\vec{r})\rangle^2$ are presented in the middle row. In all cases, the SODI reconstruction can better resolve the object. To retrieve the original values of the phase while increasing the resolution, one can also compute the phase of $\sqrt{\langle E^2(\vec{r})\rangle - \langle E(\vec{r})\rangle^2}$, which is shown in the bottom row of Fig. S4.

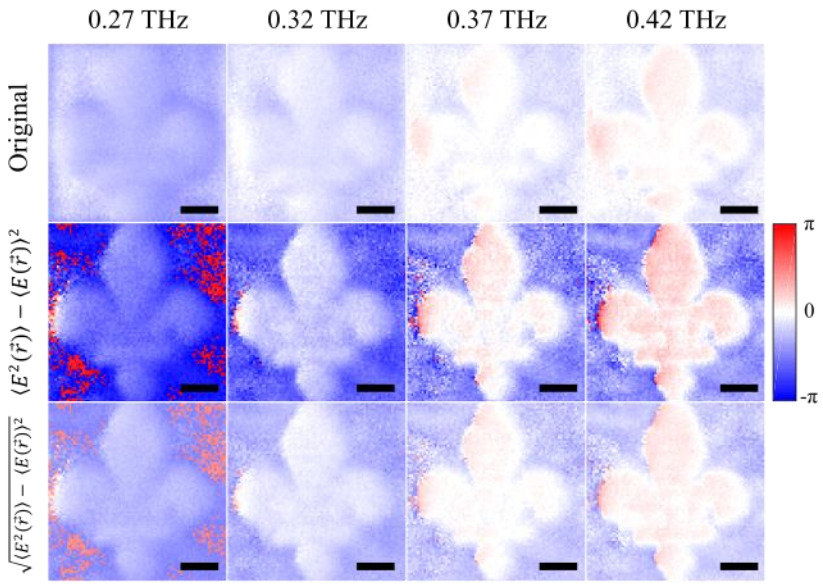

Fig. S4 Second order SODI phase reconstruction using binary amplitude masks at different frequencies. Top row: original phase images. Middle row: SODI reconstruction using $\langle E^2(\vec{r})\rangle - \langle E(\vec{r})\rangle^2$. Bottom row: SODI reconstruction using $\sqrt{\langle E^2(\vec{r})\rangle - \langle E(\vec{r})\rangle^2}$. Scale bar size is 5 mm.

E. Impact on the choice of the mesh and basis on the second-order SODI image reconstruction

In this Section, we analyze the impact of certain choices on the second-order SODI image reconstruction. In particular, we are interested in answering the three following questions: 1) For a fixed size of group of pixels, how does the number of subpixels impact the reconstruction?, 2) Considering not using all the vectors of a Hadamard basis, how does the choice of the vectors affect the reconstruction?, 3) How the shape of the subpixel (triangle, hexagon or square) impacts the reconstruction?

Impact of the number of subpixels

To judge the quality of the reconstruction, we use a binary Siemens star (Fig. S5a). As a PSF, we use a Gaussian with a width $\sigma = 1.5$ mm (Fig. S5b). The initial image was obtained by convoluting the object with the PSF and is presented in Fig. S5c. Next, to apply the SODI algorithm, we use 2x2 (Fig. S5d), 4x4 (Fig. S5e) and 8x8 (Fig. S5f) square tiles and the Hadamard basis of order 4, 16 and 64 respectively. In these simulations, the size of the group of pixels is conserved while the individual subpixels are reduced in size to accommodate more pixels. We observe in Fig. S5d-f that in all three cases the image resolution is improved because the lines of the Siemens closer to the center are better distinguishable than in the original image of Fig. S5c. However, by increasing the number of subpixels, the quality of the reconstruction is improved as can be seen by the absence of reconstruction artifacts in Fig. S5f compared to Fig. S5d.

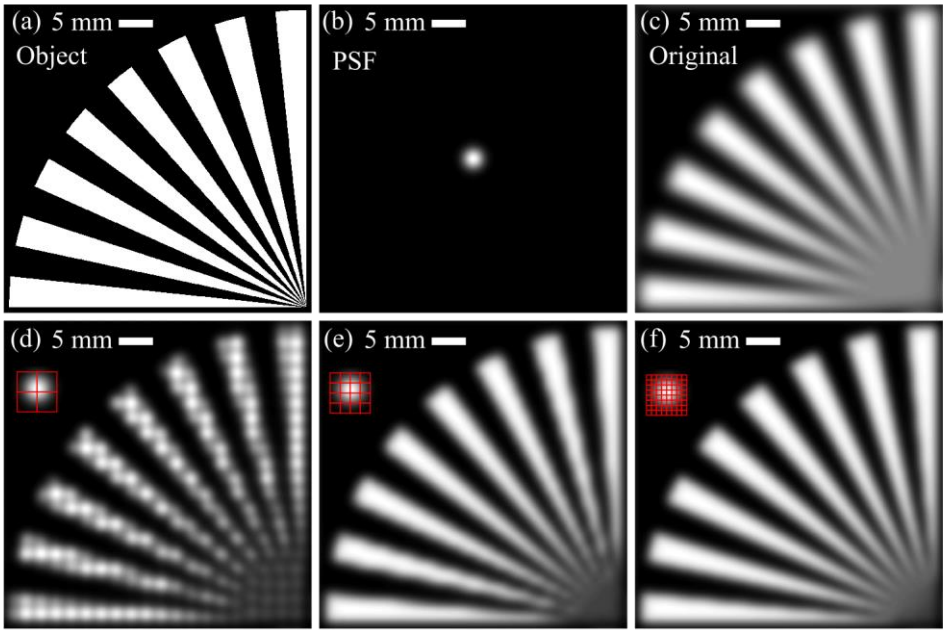

Fig. S5 (a) Object corresponding to a binary amplitude Siemens star. (b) Gaussian PSF with a width of 1.5 mm. (c) Original image obtained by convoluting the object to the PSF. (d) Second-order SODI reconstruction considering 4 pixels, (e) 16 pixels and (f) 64 pixels in the group of pixels.

Impact on the choice of the vectors of a basis

Next, considering using a basis with more vectors than the number of pixels, we are interested on evaluating the impact of the choice of a subset of vectors to reconstruct the image. For this simulation, as before, we use a Siemens star and PSF Gaussian with a width of 1.5 mm. The original image obtained by convolution of the Siemens star (Fig. S5a) with the PSF (Fig. S5b) is shown in Fig. S6a. Next, we use 3x3 square tiles and a Hadamard basis of order 16. Thus, there are fewer pixels (9) than the number of possible choices given by the Hadamard basis (16). However, this has no impact on the reconstruction because every vector of the Hadamard basis is orthogonal to all the others, meaning that the local orthogonality condition is always respected. This is confirmed by our simulations where we randomly select 9 vectors out of the 16 for the reconstruction (Fig. S6b-f). The resolution is always improved when compared to the original image and there is no effect on the particular choice on the quality of the reconstruction.

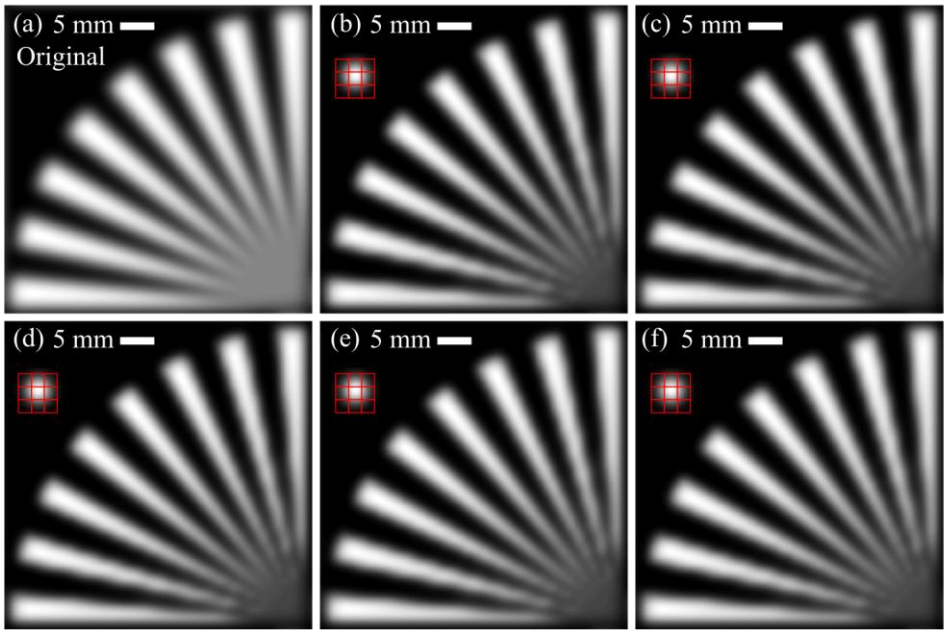

Fig. S6. (a) Original image obtained by convoluting the Siemens start with a Gaussian of width 1.5 mm. (b) Second-order SODI reconstruction using 9 randomly selected vectors of the Hadamard basis of order 16. Selected vectors are {1,2,3,6,8,9,10,13,15}, (c) {3,6,7,8,10,12,14,15}, (d) {4,5,6,8,10,12,13,14,16}, (e) {1,4,6,9,10,11,12,13,16}, (f) {2,3,4,5,7,9,11,15,16}.

Impact of the choice of the subpixel shape on the reconstruction

Finally, as we mentioned in the main paper, the subpixels are not limited to square tiling, as triangular and hexagonal tiling can also be used to cover the two-dimensional plane. To evaluate the impact of the choice of the subpixel shape we perform second-order SODI reconstruction using 6 triangles (Fig. S7ad), 7 hexagons (Fig. S7be) and 9 squares (Fig. S7cf). For these numerical simulations, we used identity matrices which correspond to successive illumination of the subpixels. As PSFs, we used Gaussian with width of 1.1 mm in Fig. S7a-c and 1.3 mm in Fig. S7d-f. In general, the choice of the pixel shape does not impact the resolution. However, the artifacts in the reconstruction depends greatly on the choice of the tiling choice, as it can be clearly seen in Fig. S7a-c where the artifacts are more visible because the relative subpixel size compared to the PSF width is not adequate.

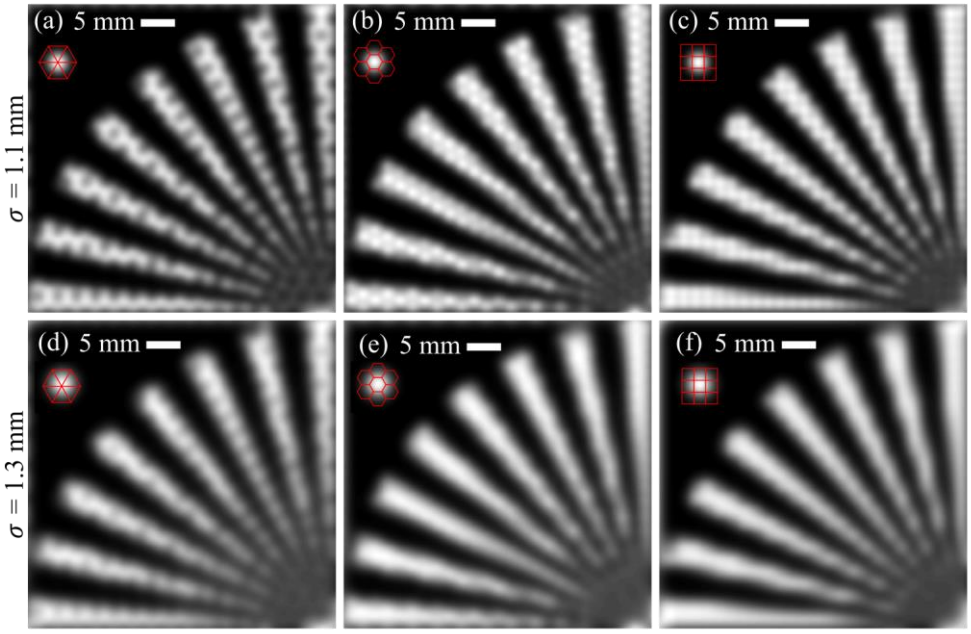

Fig. S7. Second-order SODI reconstruction using a width of (a)-(c) 1.1 mm and (d)-(f) 1.3 mm and using (a),(d) 6 triangles, (b),(e) 7 hexagons and (c),(f) 9 squares.

F. Super-resolution reconstruction of order 4

For a reconstruction of order $n = 4$, the 4th order orthogonality condition is defined as:

$$\langle M(r_1,t)M(r_2,t)M(r_3,t)M(r_4,t)\rangle_t = \frac{1}{N_t}\sum_{t=1}^{N_t} M(r_1,t)M(r_2,t)M(r_3,t)M(r_4,t) = \begin{cases} C & \text{if } r_1 = r_2 = r_3 = r_4 \\ 0 & \text{else} \end{cases} \quad \text{(S5)}$$

For the simulation result shown in Fig. 4i, we constructed a basis with $N_r = 16$ pixels. First, we note that the following basis with two pixels respect the 4th order orthogonality condition:

$$A_1 = \begin{bmatrix} -1 & -1 \\ 1 & -i \\ 1 & -1 \\ i & -1 \end{bmatrix} \quad \text{(S6)}$$

as does the following one:

$$A_2 = \begin{bmatrix} -i & -i \\ -i & -1 \\ -1 & -i \\ -1 & 1 \end{bmatrix} \quad \text{(S7)}$$

One can then verify that the Kronecker product of these two matrices leads to a new matrix that respects the 4th order orthogonality condition as well:

$$A_3 = A_1 \otimes A_2 = \begin{bmatrix} i & i & i & i \\ i & 1 & i & 1 \\ 1 & i & 1 & i \\ 1 & -1 & 1 & -1 \\ -i & -i & -1 & -1 \\ -i & -1 & -1 & i \\ -1 & -i & i & -1 \\ -1 & 1 & i & -i \\ -i & -i & i & i \\ -i & -1 & i & 1 \\ -1 & -i & 1 & i \\ -1 & 1 & 1 & -1 \\ -1 & 1 & 1 & -1 \\ 1 & -i & i & 1 \\ -i & 1 & 1 & i \\ -i & i & 1 & -1 \end{bmatrix} \quad \text{(S8)}$$

This new matrix defines N_t =16 masks containing $N_r = 4$ pixels in the basic pixel group. By continuing in a similar fashion, we can create a fourth matrix by computing the following Kronecker product:

$$A_4 = A_3 \otimes A_1 \quad \text{(S9)}$$

where A_4 has dimensions of $N_t = 64$ and $N_r = 8$ pixels. Finally, the matrix:

$$A_5 = A_4 \otimes A_2 \quad \text{(S10)}$$

has dimensions of $N_t = 256$ (number of locally orthogonal masks in a set) and $N_r = 16$ (number of pixels in the basic pixel group). We verified numerically that the new constructed matrix respects the 4th orthogonality conditions by computing all the 3876 possible distinct 4-vector products. As expected, all of them equal 0, except those when the 4 indices are the same.

Following several numerical experimentations, it seems that the Kronecker product of two matrices that respect the orthogonality condition yields a third matrix that also respect the orthogonality as well. This mathematical hypothesis has yet to be rigorously demonstrated.

References

[1] M. A. C. de Araujo, R. Silva, E. de Lima, D. P. Pereira, and P. C. de Oliveira, "Measurement of Gaussian laser beam radius using the knife-edge technique: improvement on data analysis," *Applied Optics,* vol. 48, no. 2, p. 393-396, 2009.

[2] E. Hecht, "Modern Optics: Lasers and Other Topics," in *Optics*, 4th ed., Addison-Wesley, 1998, p. 595.